Mechanical Systems and Signal Processing 118 (2019) 30–40

Contents lists available at ScienceDirect

Mechanical Systems and Signal Processing

journal homepage: www.elsevier.com/locate/ymssp

Vibration measurement using a pseudo-stereo system, target tracking and vision methods

Thomas Durand-Texte [a,b], Elisabeth Simonetto [b], Stéphane Durand [b], Manuel Melon [a,*], Marie-Hélène Moulet [c]

[a] LAUM UMR CNRS 6613, avenue Olivier Messiaen, F-72085 Le Mans cedex 9, France
[b] Laboratoire Géomatique et Foncier, CNAM, 72000 Le Mans, France
[c] Centre de Transfert de technologie du Mans, 72000 Le Mans, France

ARTICLE INFO

Article history:
Received 21 July 2017
Received in revised form 14 August 2018
Accepted 18 August 2018

Keywords:
Vibration measurement
Vision method
Single high-speed camera
Catadioptric stereo
Target tracking

ABSTRACT

A single high-speed camera pseudo-stereo system, with a four-mirror adapter, is optimised thanks to simulation, in order to measure vibrations. The measurement errors due to several sources of noise are quantified and the impact of key parameters on the measurement accuracy is analysed. A target tracking method, with removable stickers, is assessed in this context and used in combination with vision methods. The protocol is applied to measure the sub-millimeter displacement of a plate, and allows retrieving the full Frequency Response Function and associated Operational Modal Shapes. The results are compared with those obtained with reference methods using an accelerometer and a laser vibrometer. Finally, this optimised setup is used to study the relevance and potential limitations of the approach applied to an electro-acoustic source: a low-frequency loudspeaker.

1. Introduction

In the field of vibro-acoustics, the measurement of vibrations is fundamentally at stake, either to assess the dynamic behaviour of various structures [1], in terms of stress, fatigue, wave propagation. . ., or to identify and characterise the vibrating sources [2] and improve the design of mechanical parts. The most widely used tools are usually intrusive accelerometers [3] or laser vibrometers [4], which both measure single point acceleration and velocity for necessarily repeatable stationary phenomena.

When considering transient signals, acoustic methods with pressure or velocity sensor arrays may be used. They range from real-time near-field acoustic holography [5,6], to time-domain near-field equivalence source imaging [7] or time reversal imaging [8]. Some of the limitations include the high number of microphones involved, their sensitivity to ambient acoustic noise or the impact of retro-propagation errors, hence the current extensive investigation to improve them or design new protocols.

Along with these well-established approaches, several optical techniques have been successfully applied to vibro-acoustics: deflectometry [9] for real-time shape measurement, digital holography [10] for displacement measurement based on laser interferometry or photogrammetry [11] for shape, displacement or deformation measurement, for stationary or

* Corresponding author.
E-mail address: manuel.melon@univ-lemans.fr (M. Melon).

https://doi.org/10.1016/j.ymssp.2018.08.049
0888-3270/

dynamic phenomena [12,13]. In the matter, Baqersad and al. [11] thoroughly described the technological advance in methods based on photogrammetry applied to the vibration measurement of less accessible systems such as bridges [14–16], rotating systems [17,18] or even plane wings in wind tunnels [19]. Yang et al. [20] proposed a blind identification method based on video measurements to characterize bench-scale structures.

The photogrammetric protocols usually aim at retrieving the Operational Modal Shapes (OMSs); most have a scope limited to stationary or in-plane variations if one single camera is used, and involve a huge quantity of data, long processing time and extra post processing (with the Finite Element Method (FEM) for example [21]) with generally inadequate software [11]. The most widely used techniques for full-field 2D (or 3D) displacement measurement are the (Stereo) Digital Image Correlation methods (DIC & SDIC) [22], which require two points of view originally obtained from two high-speed cameras. In order to avoid the related problems of cost and synchronisation, studies have led to the design of the now conventional single camera pseudo-stereo system also called catadioptric stereo system [23], which splits the CCD/CMOS sensor of the camera into two halves, thanks to a four-mirror adapter, to capture the stereo views [24,25] (for a detailed review see [26]).

Recently, this system was used to measure adiabatic shear bands [27] from 2D in-plane displacement, using the measurement of the out-of-plane displacement to improve the accuracy of the calculations. Yu and Castellini [28,29] studied the relevance of this setup for the modal analysis of a plate and a beam.

Concerning dynamic 3D vision, several commercial systems with two or more cameras are available on the market. Among them, those from GOM and Correlated Solutions have been tested for vibration measurements respectively on a plate [30] or on a beam [31]. However, these systems require at least two cameras that are expensive and may lead to synchronisation problems. So, the authors of the present article carried out preliminary work with a single camera set-up on the measurement of transient vibratory deformation [32], and on the accuracy of the measurement [33], including the impact of key parameters thanks to Blender-simulated images [34].

This paper now focuses on the experimental validation of an optimised version of the conventional pseudo-stereo setup, applied to measure the vibrations of a plate and of an electro-acoustic source. As this paper focuses on applications of 3D vision systems in vibro-acoustics, these two classical sound sources were chosen. Indeed, they can be found in many common products: machine or car bodyworks, sound-control enclosures, loudspeaker systems, etc. Instead of the usual speckle pattern and (S) DIC method, the authors, for the present article, chose to assess the use of targets printed on removable stickers in combination with a target tracking method. This allows keeping a large angle between the virtual cameras and the measured object, thus minimising the uncertainty, and may be particularly suited for some types of measurement typically involving musical instruments, for which a permanent pattern is not relevant. To summarise, compared to the existing scientific literature or commercial set-ups, this article proposes a single-camera system using target tracking. This solution allows reducing the cost of the system and using large angles between the two virtual cameras, thus improving the accuracy of the vibration measurement.

This paper is organised as follows: Section 2 deals with the simulation stage, experimentally quantifies the measurement errors due to several sources of noise, and sets the impact of key parameters on the accuracy of the measurement before establishing the choice of the optimised parameters for the defined target. Section 3 reports the experimental validation of the setup applied to a vibrating plate, for the full Frequency Response Function (FRF) and OMSs, and compares these results with those obtained with an accelerometer and a laser vibrometer. Section 4 experimentally studies the relevance and potential limitations of the approach applied to a low frequency loudspeaker.

2. Protocol, error sources and accuracy

The setup is based on the conventional pseudo-stereo system, involving a single very high-speed camera (12,500 frames per second) and a four-mirror adapter. Two virtual cameras are generated from a real one, at the expense of the number of pixels per view, which is thus divided by two (Fig. 1a).

The configuration of this system is optimised by using a simulation model, as close as possible to the real experimental setup and available equipment, designed to be applied to the displacement measurement of a vibrating plate and of an electro-acoustic source. As mentioned previously, the target tracking method (with removable stickers) is tested in this paper. This choice impacts key parameters: the pattern of the target, the angle between the virtual cameras and the object, and the detection method, which have then to be chosen carefully. The analysis of the impact of these parameters on the measurement accuracy finally leads to select the configuration that minimises the error. The synoptic of the approach used is shown in Fig. 1b.

i. The first step of the protocol consists in simulating images of a calibration target and of a vibrating plate, with Blender software, using the cycle render (ray tracing solver) [34]. A simulated camera is thus set, with a 1024×1024 pixel matrix, with a focal length of 50 mm for the optical objective, and a 2% radial lens distortion for the images. The size of the pixels is 20 micrometers. The simulated lateral mirrors are 200 mm $\times$ 200 mm large and the central knife-edge right-angled prism mirror is 25 mm large.

ii. The second step is linked to the detection of the targets on the calibrating pattern and on the vibrating plate. Four techniques have been tried and tested: the universal weighted centroid method, the blob detector implemented in OpenCV [35], based on contour detection [36], a least square ellipse fitting algorithm [37] and a dual ellipse estimator [38]. Previous work [33] showed that, among the four detection algorithms tested, the results obtained with the blob detector had the

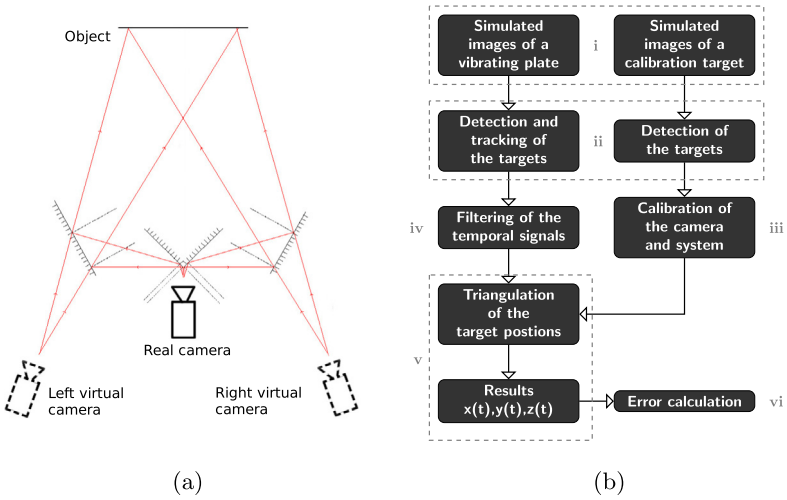

Fig. 1. (a) Schematic representation of the pseudo-stereo system and (b) Synoptic of the simulation process.

maximum error. Moreover, the universal weighted centroid method was the most sensitive to the noise in the images. These two algorithms are considered inadequate for the present objective, and thus ruled out in this paper. As regards the target pattern, the use of the standard "point" with a small number of pixels leads to aliasing in the images, as shown in Fig. 2a. If the pattern follows a Gaussian profile, the gray scale gradient seems better described but the quantity of energy is limited (Fig. 2b). For this study, a mix of the two patterns, *i.e.* a point with Gaussian-shaped borders (Fig. 2) (labelled "Gaussian-point" in the present article) is used, thus limiting aliasing and maximising the quantity of energy, as previous simulations showed that it resulted in performing better detection [33]. Besides, the choice of the tracking method results in speeding up the detection stage, as tracking is basically done after detecting and sorting the locations of the targets in the first image with no extra processing required for each subsequent image.

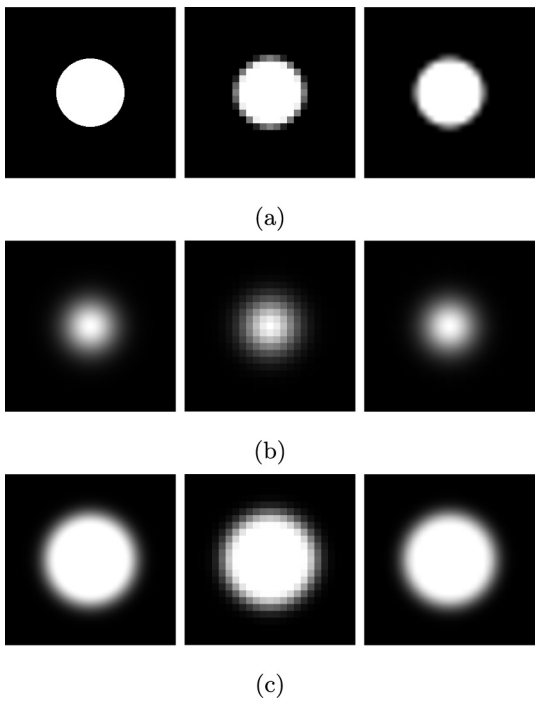

Fig. 2. Images of patterns with different resolutions (a) point, (b) Gaussian profile (c) Gaussian-point; (first column) 300 × 300 pixels, (second column) down sampled to 25 × 25 pixels, (third column) up sampled back to 300 × 300 pixels.

iii. The third step is about the calibration of the camera and the system, with the calibration tools implemented in OpenCV [35]. Calibration is first carried out only on the "real" camera, then on the stereoscopic system, by adjusting the intrinsic parameters of the virtual cameras to the values retrieved for the "real" one, thus minimising the errors by reducing the number of parameters to be set simultaneously and setting two identical virtual cameras.

iv. The fourth step aims at reducing the effects of noise in the triangulated results. The retrieved temporal signals of the target locations in the images are thus filtered with a fourth-order low pass Butterworth filter.

v. Once these two last steps completed, the triangulation of the target positions can be performed [39] and results obtained in the time domain for the three axes of space, which allows measuring small displacements.

vi. Finally, the impact of the key parameters on the error is studied and leads to the approximate quantification of the accuracy on an imposed rigid body displacement. On the one hand, for the sake of simplicity, the sampling frequency of the camera (f_s) is set to 1 and the simulated reference displacement signal is the sum of three sines, with frequencies equal to $f_s/50, f_s/10$ and $f_s/4$ and amplitudes equal to 120 μm, 70 μm and 100 μm respectively. On the other hand, in order to go further and to understand better the other error sources, specific data linked to the vibration of the camera, the non-planarity of the mirrors, the noise in the image or the flaws in the calibration target are experimentally extracted and injected in the simulation model to achieve a more realistic view. This second simulation step results in setting the optimised configuration of the system for a sub-millimeter displacement measurement.

2.1. Experimental sources of error

Regarding the sources of error, four hypotheses are formulated, linked to the imperfection of the camera, of the mirrors, of the images and of the calibration target. Specific data are thus extracted from experimental measurement, confirming the assumptions, in order to enhance the simulation model and optimise the real protocol.

Vibration of the camera The very high-speed camera is placed on a robust tripod in front of a static plate with targets, in order to measure indirectly the vibration of the camera due, in this case, to its four fans. Knowing the dimension of the plate, its distance to the camera, the number and size of the pixels, and the variations of the positions of the targets in the images, the approximate displacement of the camera, without excitation signal, can be calculated thanks to the usual pinhole camera model [39]. The results obtained in the frequency domain lead to two conclusions. Firstly, the localised sharp peaks very likely come from the vibration of the camera, whereas the broadband noise necessarily comes from the noise in the images. For the configuration tested, the amplitudes of displacement for the peaks range from 0.1 μm to 0.5 μm and occur at several potentially harmonic frequencies. Secondly, experimental tests have shown that, according to the exact location and orientation of the stand, the frequency peaks are more or less visible, and not systematically in the same directions of space; however, the amplitude of the displacement remains inferior to 0.5 μm in all cases (cf. Fig. 5 *infra*).

Optical mirrors. When analysing the epipolar distances on all the regularly spaced measurement points, local increases can be noticed (up to 2 pixels, resulting in an error approximately equal to 500 μm), most probably due to the impact, on the image, of the non-planarity of the mirrors, given the high quality of the optics and the lack of distortion-correlated variations in the calculated map of the epipolar distances (the surface flatness of the mirrors, given in the data sheet, is equal to 5 λ at 632 nm).

Noise in the images. After analysing the statistical variation of the grey scale value (GSV) of the pixels in 200 subsequent images of the front view of a static plate, the observed noise in the images may, in our case, be interpreted as and thus modelled as the sum of a Gaussian noise ($\sigma_G = 0.3$ in GSV; usually labelled "additive noise") and a photon noise ($\sigma_P(u,v) = \sqrt{I(u,v) * 255/n_e}$ in GSV, with $I(u,v)$ the GSV of a pixel, 255 the maximal value with 8 bits and n_e the number of electrons for the fully loaded sensor; usually called "multiplicative noise" in image processing). This noise results, in the frequency domain, in a broadband noise inferior to $5e-4$ pixels in the detection signals.

Calibration target. The calibration target is made up of a 297 mm × 297 mm sticker glued on a 8-mm-thick aluminium plate. When comparing the positions of the targets measured with the pseudo-stereo system to those of an ideally perfect calibration pattern, the standard variations of the triangulated positions, for all 8 × 8 target points, for the three axes of space are: $\sigma_x \approx 160$ μm, $\sigma_y \approx 100$ μm and $\sigma_z \approx 330$ μm. The different values for the $\vec{x}$ and $\vec{y}$ axes may be due to the printing stage, done line after line by the ink-jet A3 printer. The variation for the $\vec{z}$ axis may come from the non-flatness of the plate. But in all cases, these experimental measurements necessarily include a degree of uncertainty, also linked to the non-planarity of the mirrors.

Conclusion. Firstly, the vibration of the fans of the camera induces a relatively small stationary error, which is easy to identify and take into account in the measured response. The impact of the non-planarity of the mirrors is quantified but not the non-planarity itself. This spatially stationary error clearly impacts the shape measurement but becomes negligible for the measurement of very small displacements, according to the empirical observations. As a result, these two first sources of error are not taken into account in the simulated model, but are kept as relevant information for the analysis of the experimental data.

Secondly, the noise in the images follows the Gaussian and photon noise models and is thus easily added to the simulated images. In the same way, an error corresponding to the standard variation of the triangulated positions of the targets is injected into the model for the calibration calculation, which allows keeping a simulated perfect calibration target (for more details, see [40]).

2.2. Simulations

This present paper focuses on the comparison between the ellipse fitting algorithm and the dual ellipse estimator (cf. 2.ii), in terms of detection accuracy, with a "realistic" noise added to the simulated images and the positions of the targets in the calibration rig, *i.e.* in a context similar to the experimental observations.

Fig. 3 shows the results of this simulation stage: the average and maximum values of the standard deviation of the difference between the measured and the reference signals for both detectors, for angles ranging from 30° to 55°, for all measurement points, while keeping a roughly constant width for the images of the plate. The choice of these limit angles is linked to the size of the optical table, in our case 1 m wide, and to the increased difficulty, for smaller or larger angles, in positioning correctly the optical components of the setup to get valid images of the studied object.

From this simulation, two main conclusions can be drawn: firstly, the average and maximum values of the error are lower for the dual ellipse estimator for all the angles. Secondly, the higher the angle is, the lower the uncertainty is for the tested angles.

2.3. Optimised configuration

According to the results of the simulation stage, the optimised configuration for the vibration measurement with the conventional pseudo-stereo system and a target tracking approach is thus:

- a Gaussian-point pattern for the targets to maximise the quantity of energy and minimise aliasing in the images;
- the use of the dual ellipse estimator, considered as the best suited in our context;
- the choice of the largest angle possible between the virtual cameras and the object.

NB: The flaws in the calibration target and the induced error in calibration seem to have a negligible impact on the vibration measurement. According to the experimental observations, the non-planarity of the mirrors and the use of large angles impact shape measurement but have a negligible impact on small displacement measurement.

3. Experimental validation of the setup applied to a vibrating plate

3.1. Setup

The very high-speed camera is fastened to a robust tripod and faces a silver-coated knife-edge right-angled prism mirror (25 mm × 25 mm large). The two lateral aluminium-coated mirrors, sized 200 mm × 200 mm, are set on rotary stages on an optical rail.

In agreement with the simulation results, the angles of the mirrors are set to get the following angles between the virtual cameras and the object: (left) ≈ 50°; (right) ≈ 57°. The asymmetry in the values allows maintaining the optimal size of the images on the pixel matrix of the real camera, while positioning all the optical and lighting components. Secondly, the sticker glued on the plate is made of 31 × 31 targets with a Gaussian-point pattern, resulting in an available measuring area of 300 mm × 300 mm.

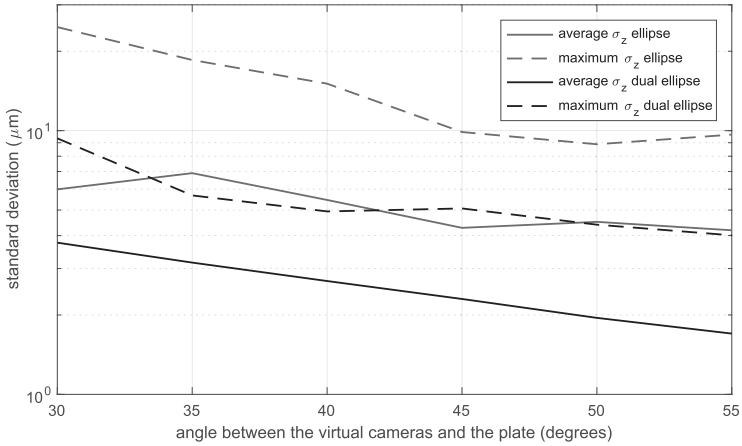

Fig. 3. Average and maximum values of the standard deviation of the error along the $\vec{z}$ axis, with the ellipse fitting algorithm and the dual ellipse estimator.

The four-mirror adapter and a 200 W LED spot are positioned on a large vibration-isolated optical table; the plate, fastened at its four corners on a stand, is positioned on a second vibration-isolated optical table, placed on top of the first one. Fig. 4 shows a picture of the experimental setup.

A is set at the back of the plate in order to generate the excitation required for the measurement; an impedance head including a force sensor and an accelerometer is inserted between the two (205 mm from the top and 135 mm from the left side of the plate). The applied signal is a swept sine ranging from 20 Hz to 2,500 Hz during 3.5 s to maximise the displacement at each frequency.

3.2. Background noise

A first series of 10,000 images is acquired (f_s = 12,500 Hz) without any excitation signal, to get information on the background noise and the related uncertainty. In the time domain, the average standard deviation of the reconstruction error for the $\vec{z}$ axis is: σ_z = 1.50 µm. This value is in the same range as the figure obtained in the simulation, while including the error due to the vibration of the camera, which was not directly taken into account in the simulation model. In the frequency domain, the signal amplitudes for all the frequencies (including the noise due to the vibration of the camera), calculated from the Power Spectrum Density (PSD) are shown in Fig. 5.

The peaks on the curves correspond to the vibration of the camera; the axes $\vec{x}$ and $\vec{y}$ seem more impacted. For the $\vec{z}$ axis, the background noise is louder from 60 Hz to 100 Hz, with amplitudes close to 0.3 µm.

3.3. Frequency Response Function (FRF)

The full FRF obtained with our method is compared to the results given by the accelerometer of the impedance head. Fig. 6 shows, first, that the shapes and amplitudes of the peaks are similar on both curves, which validates the protocol used. Secondly, the results in Fig. 7 show that the smaller the displacement, the higher the noise, which sets a limitation for the investigation of deeps in displacement and the highest frequencies. The background noise only impacts displacement amplitudes inferior to a few microns.

When analysing the spectrogram calculated for the measurement point of the accelerometer on the plate (Fig. 8), the frequencies corresponding to the vertical lines clearly match the peaks identified in Fig. 5 and are due to the vibration of the camera. This may in turn be taken into account in the analysis of the FRF results (Fig. 6).

3.4. Modal shapes

The OMSs retrieved from the measurement with the pseudo-stereo system are compared with those obtained with a laser vibrometer. The results are displayed in Fig. 9, for three resonance frequencies and one intermediary frequency, and globally show a good agreement up to 660 Hz when the signal-to-noise ratio is favorable (a 98.8% and 97.4% correlation at 36 Hz and 66 Hz respectively, a 91.5% correlation at 520 Hz and a 72.5% correlation at 660 Hz).

The slight variations are linked to the experimental conditions: for practical reasons, the measurement with the laser vibrometer took place in a different place, with a higher room temperature.

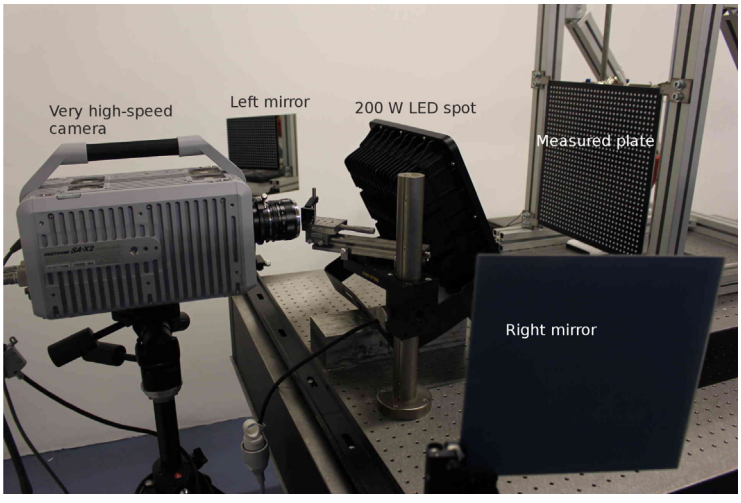

Fig. 4. Picture of the experimental setup.

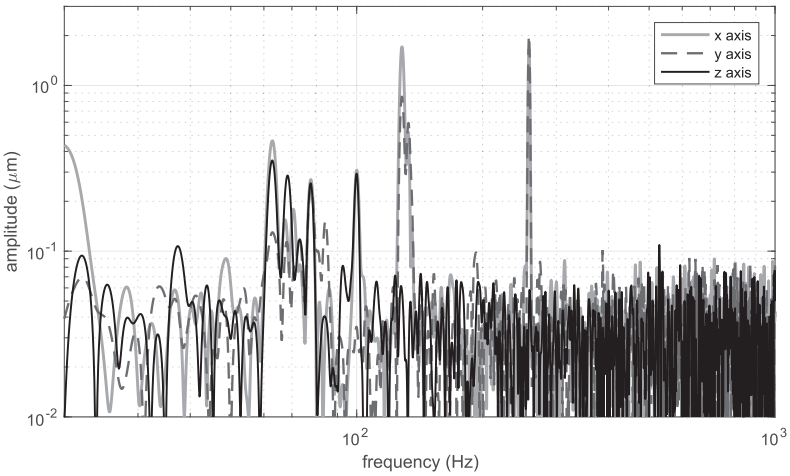

Fig. 5. Measured displacement along the three axes of space without excitation signal.

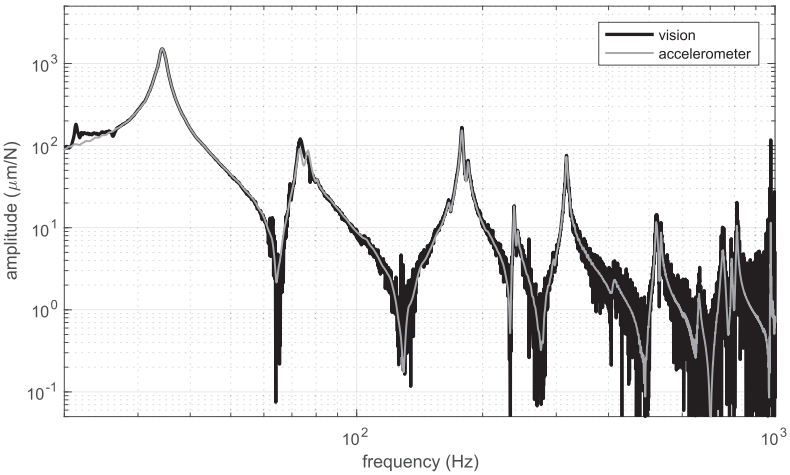

Fig. 6. Measured Frequency Response Functions along the $\vec{z}$ axis.

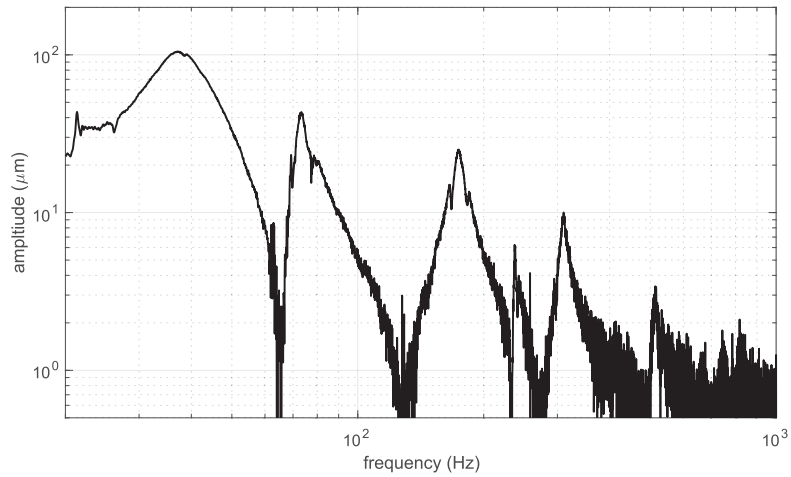

Fig. 7. Measured Power Spectral Density along the $\vec{z}$ axis.

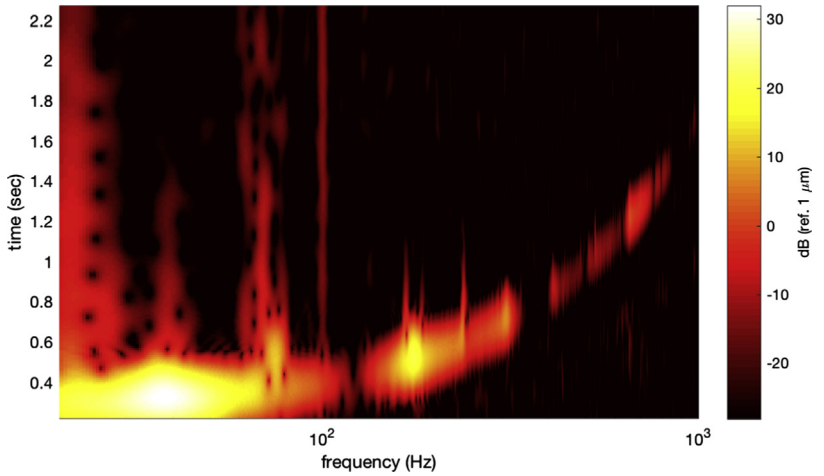

Fig. 8. Spectrogram of the signal measured at the position of the impedance head on the plate (dB Ref. 1 μm).

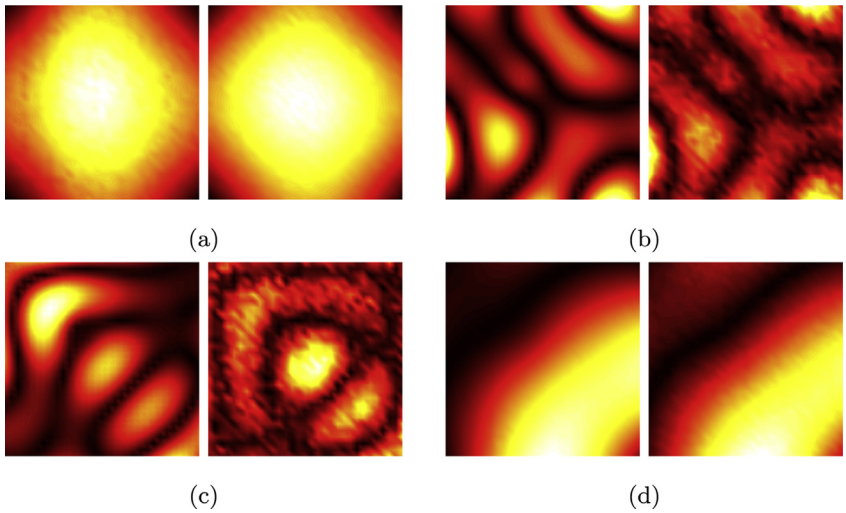

Fig. 9. Operational Modal Shapes measured on 31 × 31 points, spaced 10 mm: (a) mode at 36 Hz, (b) mode at 520 Hz, (c) mode at 660 Hz, (d) response at 66 Hz, (left: vibrometer, right: vision).

3.5. Conclusions

The results obtained show that the setup and protocol are adapted to measure sub-millimeter displacement but the system reaches a limitation for displacement amplitudes inferior to a few micrometers, notably because of the background noise. The FRF curve and the OMSs are coherent with those obtained with current reference methods, with a cut-off frequency of about 700 Hz in the present configuration, which experimentally validates the approach presented in this paper.

4. Application to an electro-acoustic device: a loudspeaker

As the setup and protocol are experimentally validated for the vibration measurement, the objective is now to carry out a preliminary study on a well-known vibrating electro-acoustic device, a low-frequency loudspeaker, to get insight on the relevance and potential limitations of our approach in this context.

The setup used to measure the vibration of the plate is tuned to the characteristics of this new object of study. The angles of the mirrors are set experimentally and give the following angles between the virtual cameras and the object: (left) $\approx 28^\circ$; (right) $\approx 38^\circ$ (cf. 3.1 for more details on the asymmetry of the values). The main difference comes from the nature of the object itself, notably its non-planarity and circular shape, which directly impacts the choice of the pattern: here, 24 lines

Fig. 10. Picture of the loudspeaker viewed through the pseudo-stereo system.

of 6 points are stuck on the cone and 8 lines of 3 points plus 1 point are stuck on the dome, generating a star-like pattern. An image of the loudspeaker viewed through the pseudo-stereo system is shown in Fig. 10.

4.1. Frequency Response Function

A swept sine is applied to the speaker, ranging from 20 Hz to 430 Hz, with 1 V of amplitude. The protocol defined for the vibration measurement of the plate is used in this case too and the FRF is calculated thanks to two different methods: firstly by using the PSDs with the H1 estimator, secondly by using adaptive filtering [41], and more precisely the single channel Wiener filter. These results are compared to those obtained with a laser vibrometer (the applied signal is, in this case, a swept sine, ranging from 20 Hz to 2,500 Hz, during 3 s, with $\approx$ 300 mV of amplitude). Fig. 11 shows the three curves for the point delineated in Fig. 10.

Four conclusions can be drawn. Firstly, the results obtained with the vision protocol are coherent with those obtained with the laser vibrometer as the two curves are similar. Secondly, the use of adaptive filtering enhances the results and clearly reduces the noise in the FRF, notably for the highest frequencies. Thirdly, the vibration of the camera visibly impacts the results but only around 20 Hz. Fourthly, the slight variations between the two curves are due to the slight variations in the location of the measurement points for the two methods and the different experimental conditions (cf. 3.4), which, in turn, induces a slight shift in the modal frequencies.

4.2. Modal shapes

In the context of this preliminary study, the objective is to analyse the potential relevance of the approach on the vibration measurement of a speaker. As a consequence, the OMSs obtained with the present vision protocol are compared to those obtained with a laser vibrometer. Fig. 12 shows the results for two modal frequencies visible in the FRF (97 Hz and 309/316

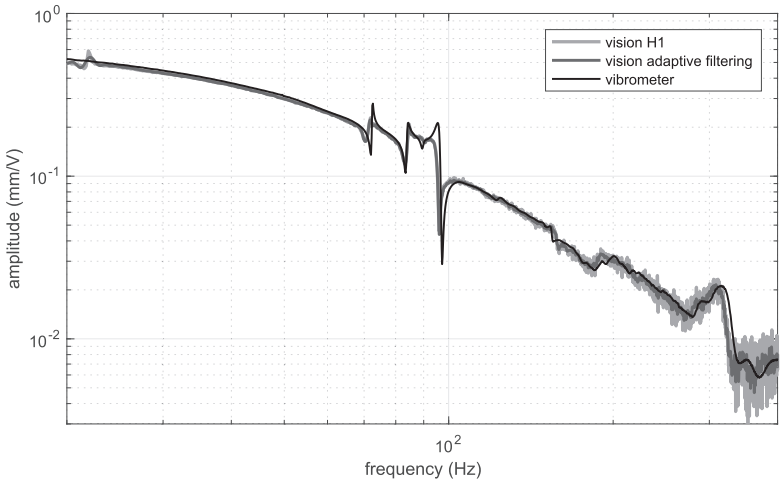

Fig. 11. Frequency Response Functions of the speaker for a side point.

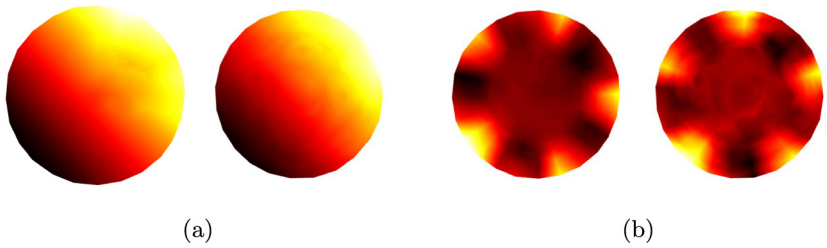

Fig. 12. Measured Operational Modal Shapes: (a) mode at 97 Hz, (b) mode at 309/316 Hz (left: vibrometer, right: vision).

Hz; cf. Fig. 11). The pseudo-stereo setup and presented vision protocol are clearly relevant for the vibration measurement of a low frequency loudspeaker, as shown by the similar results obtained with this usual reference method. The first modes are visible on the three axes of space, which is obviously an asset of the vision approach. However, the number of measurement points is clearly insufficient to correctly describe more complex radial modes: for the 309/316-Hz mode, typically, 5 wavelengths are visibly described, with only 24 points, which corresponds to less than 6 points per wavelength and leads to a spatial interpolation error greater than 3%.

5. Conclusions

Firstly, the use of the presented optimised single camera pseudo-stereo system in combination with the target tracking method is validated experimentally for vibration measurement, as proven by the successful measurement of the sub-millimeter displacement of a planar and a non-planar object, in a context of repeatable phenomena. This opens up onto the possibility of full-field measurement for non-reproducible events.

Secondly, optimising the setup went hand in hand with designing a simulation model taking into account several sources of noise, which allowed reliably predicting the uncertainty measured experimentally ($\sigma_z \approx 1.5$ µm). Further study including the technological characteristics of the newly-released very-high speed cameras (the higher number of pixels or the "quiet fan" option for example) or focusing on how the variation of the focal length may impact the accuracy of the method, could lead to even more accurate results.

Thirdly, the use of the target tracking method is relevant and allows keeping large angles between the cameras, with a degradation of the measured shape but no visible damaging impact on the measurement of sub-millimeter displacement, which validates its use for vibration measurement. The main asset of the approach is that it does not alter permanently the studied object and may be safely applied, in acoustics, to the study of musical instruments for example.

Finally, in the field of electro-acoustics, and more particularly in the case of a loudspeaker membrane, the mass of the stickers is, however, probably no longer negligible and might impact the results in some degree. Besides, the tested star-like pattern induces a target density that seems too low to analyse the more complex radial modes. As a consequence, one of the key parameters requiring further investigation is the choice of the pattern and notably the targets distribution in order to enhance the protocol and adapt it to the characteristics and behaviour of this specific object and pursue the analysis of the application of this vision protocol to the field of electro-acoustics. To sum-up, the experimental set-up presented here could be used to provide displacement data for inverse characterization methods. It will then allow to estimate the modal [42] or material (i.e. Young's modulus, Poisson's Ratio, etc.) parameters of the device under test (DUT) or the force applied to it [2]. Concerning direct methods, another application would be the calculation of the acoustic field radiated by the DUT using a Boundary Element Method thus giving frequency responses at given locations or 3D directivity patterns.

Acknowledgements

The work presented here is supported by the institute "Le Mans Acoustique" and funded by the "Pays de la Loire" region and the "European Regional Development Fund". The authors wish to thank Mathieu Sécail-Géraud and James Blondeau for their help on the laser measurements.

References

[1] D. Ewins, Modal Testing: Theory, Practice, and Application, Mechanical Engineering Research Studies: Engineering Dynamics Series, Research Studies Press, 2000.
[2] C. Pezerat, J. Guyader, Force analysis technique: reconstruction of force distribution on plates, Acta Acustica United Acustica 86 (2) (2000) 322–332.
[3] B. Anders, Noise and Vibration Analysis: Signal Analysis and Experimental Procedures, Wiley, 2011.
[4] F. Frank, J. Walker, Advanced Applications in Acoustics, Noise and Vibration, CRC Press, 2004.
[5] J. Hald, Time domain acoustical holography and its applications, Sound Vibr. 35 (2) (2001) 16–25, doi:35-16:25.
[6] J.-H. Thomas, V. Grulier, P. Paillasseur, J.-C. Pascal, J.-C. Le Roux, Real-time near-field acoustic holography for continuously visualizing nonstationary acoustic fields, J. Acoust. Soc. Am. 3554–3567. doi:10.1121/1.3504656.
[7] M. Bai, J.-H. Lin, Source identification system based on the time-domain neareld equivalence source imaging: Fundamental theory and implementation, J. Sound Vib. 307 (1–2) (2007) 202–225, 307:202-225.

[8] S. Lobreau, E. Bavu, M. Melon, Hemispherical double-layer time reversal imaging in reverberant and noisy environments at audible frequencies, J. Acoust. Soc. Am. 137–2 (2015) 785–796.
[9] A. Berry, O. Robin, Identification des excitations sur des panneaux par la mesure de leur réponse vibratoire et la méthode des champs virtuels, in: CFA 2016, Le Mans, France, 2016.
[10] J. Poittevin, P. Picart, C. Faure, F. Gautier, C. Pézerat, Multi-point vibrometer based on high-speed digital in-line holography, Appl. Opt. 54 (11) (2015) 3185–3196, https://doi.org/10.1364/AO.54.003185.
[11] J. Baqersad, P. Poozesh, C. Niezrecki, P. Avitabile, Photogrammetry and optical methods in structural dynamics – a review, Mech. Syst. Signal Process. 86 (2017) 17–34, https://doi.org/10.1016/j.ymssp.2016.02.011.
[12] V. Tiwari, M.A. Sutton, S. McNeill, Assessment of high speed imaging systems for 2d and 3d deformation measurements: Methodology development and validation, Exp. Mech., doi:10.1007/s11340-006-9011-y.
[13] E. Zappa, P. Mazzoleni, A. Matinmanesh, Uncertainty assessment of digital image correlation method in dynamic applications, Opt. Lasers Eng. 56 (2014) 140–151.
[14] P. Olaszek, Investigation of the dynamic characteristic of bridge structures using a computer vision method, Measurement 25 (3) (1999) 227–236, https://doi.org/10.1016/S0263-2241(99)00006-8.
[15] M. O'Byrne, B. Ghosh, F. Schoefs, D. O'Donnell, R. Wright, V. Pakrashi, Acquisition and analysis of dynamic responses of a historic pedestrian bridge using video image processing, J. Phys: Conf. Ser. 628 (1) (2015) 012053.
[16] D. O'Donnell, R. Wright, M. O'Byrne, A. Sadhu, F. Edwards Murphy, P. Cahill, D. Kelliher, B. Ghosh, F. Schoefs, A. Mathewson, E. Popovici, V. Pakrashi, Modelling and testing of a historic steel suspension footbridge in ireland, Proc. Inst. Civ. Eng. – Bridge Eng. 170 (2) (2017) 116–132, https://doi.org/10.1680/jbren.15.00047.
[17] B. Stasicki, F. Boden, In-flight measurements of aircraft propellers deformation by means of an autarkic fast rotating imaging system, in: International Conference on Experimental Mechanic 9302, doi: 10.1117/12.2081393.
[18] M. Ozbek, D.J. Rixen, O. Erne, G. Sanow, Feasibility of monitoring large wind turbines using photogrammetry, Energy 35 (12) (2010) 4802–4811, https://doi.org/10.1016/j.energy.2010.09.008.
[19] S.S. Graves, A.W. Burner, J.W. Edwards, D.M. Schuster, Dynamic deformation measurements of an aeroelastic semispan model, J. Aircraft 40 (5) (2003) 977–984, https://doi.org/10.2514/2.6883.
[20] Y. Yang, C. Dorn, T. Mancini, Z. Talken, S. Nagarajaiah, G. Kenyon, C. Farrar, D.M. Nas, Blind identification of full-field vibration modes of output-only structures from uniformly-sampled, possibly temporally-aliased (sub-nyquist), video measurements, J. Sound Vib. 390 (2017) 232–256, https://doi.org/10.1016/j.jsv.2016.11.034.
[21] W. Wang, J.E. Mottershead, A. Ihle, T. Siebert, H. Reinhard Schubach, Finite element model updating from full-field vibration measurement using digital image correlation, J. Sound Vibr. 330 (8) (2011) 1599–1620, https://doi.org/10.1016/j.jsv.2010.10.036.
[22] M.A. Sutton, J.J. Orteu, H. Schreier, Image correlation for shape, motion and deformation measurements: basic concepts, theory and applications (2009).
[23] J. Gluckman, S.K. Nayar, Catadioptric stereo using planar mirrors, Int. J. Comput. Vision 44 (1) (2001) 65–79, https://doi.org/10.1023/A:1011172403203.
[24] M. Inaba, T. Hara, H. Inoue, A stereo viewer based on a single camera with view-control mechanisms, in: Proceedings of 1993 IEEE/RSJ International Conference on Intelligent Robots and Systems, IROS 1993, Tokyo, Japan, July 26–30, 1993, 1993, pp. 1857–1865. doi:10.1109/IROS.1993.583888.
[25] R. Wang, X. Li, Y. Zhang, Analysis and optimization of the stereo-system with a four-mirror adapter, J. Eur. Opt. Soc. – Rapid Publ. 3 (0).
[26] J. Li, X. Dan, W. Xu, Y. Wang, G. Yang, L. Yang, 3d digital image correlation using single color camera pseudo-stereo system, Opt. Laser Technol. 95 (2017) 1–7, https://doi.org/10.1016/j.optlastec.2017.03.030.
[27] T.G. White, J.R.W. Patten, K.-H. Wan, A.D. Pullen, D.J. Chapman, D.E. Eakins, A single camera three-dimensional digital image correlation system for the study of adiabatic shear bands, Strain 53 (3). doi:10.1111/str.12226.
[28] L. Yu, B. Pan, Single-camera high-speed stereo-digital image correlation for full-field vibration measurement, Mech. Syst. Signal Process. 94 (2017) 374–383 (Complete).
[29] P. Castellini, P. Chiariotti, M. Martarelli, E. Zappa, A. Lavatelli, Experimental Modal Analysis on Vibration Data Measured by Digital Image Correlation, Springer International Publishing, Cham, 2017, https://doi.org/10.1007/978-3-319-54735-030, pp.285–291.
[30] P.L. Reu, D.P. Rohe, L.D. Jacobs, Comparison of dic and ldv for practical vibration and modal measurements, Mech. Syst. Signal Process. 86 (2017) 2–16, https://doi.org/10.1016/j.ymssp.2016.02.006, full-field, non-contact vibration measurement methods: comparisons and applications.
[31] T.J. Beberniss, D.A. Ehrhardt, High-speed 3d digital image correlation vibration measurement: recent advancements and noted limitations, Mech. Syst. Signal Process. 86 (2017) 35–48, https://doi.org/10.1016/j.ymssp.2016.04.014, full-field, non-contact vibration measurement methods: comparisons and applications.
[32] T. Durand-Texte, E. Simonetto, S. Durand, P. Picart, M.-H. Moulet, M. Melon, Mesure de déformations vibratoires par vision 3d, in: CFA 2016, Le Mans, France, 2016.
[33] T. Durand-Texte, E. Simonetto, S. Durand, M. Melon, M.-H. Moulet, Estimation des incertitudes d'une méthode de mesure de déformées vibratoires par vision 3d, Instrumentation, Mesure, Métrologie 16 (1–2) (2017) 71–95.
[34] Blender Foundation, Blender 2.76b – a 3d modelling and rendering package,http://www.blender.org (nov 2015)
[35] G. Bradski, Open Computer Vision, OpenCV, Dr. Dobb's Journal of Software Tools.
[36] S. Suzuki, K. Abe, Topological structural analysis of digitized binary images by border following, j-CVGIP 30 (1) (1985) 32–46.
[37] A. Fitzgibbon, M. Pilu, R.B. Fisher, Direct least square fitting of ellipses, IEEE Trans. Pattern Anal. Mach. Intell. 21 (5) (1999) 476–480, https://doi.org/10.1109/34.765658.
[38] J.-N. Ouellet, P. Hébert, A simple operator for very precise estimation of ellipses, in: CRV '07: Proceedings of the Fourth Canadian Conference on Computer and Robot Vision, IEEE Computer Society, Montréal, Qc, Canada, 2007, pp. 21–28.
[39] R.I. Hartley, A. Zisserman, Multiple View Geometry in Computer Vision, second ed., Cambridge University Press, 2004.
[40] Z. Zhang, A flexible new technique for camera calibration, IEEE Trans. Pattern Anal. Mach. Intell. 22 (11) (2000) 1330–1334, https://doi.org/10.1109/34.888718.
[41] B. Widrow, J.R. Glover, J.M. McCool, J. Kaunitz, C.S. Williams, R.H. Hearn, J.R. Zeidler, J.E. Dong, R.C. Goodlin, Adaptive noise cancelling: principles and applications, Proc. IEEE 63 (12) (1975) 1692–1716, https://doi.org/10.1109/PROC.1975.10036.
[42] R. Huňady, M. Hagara, A new procedure of modal parameter estimation for high-speed digital image correlation, Mech. Syst. Signal Process. 93 (2017) 66–79, https://doi.org/10.1016/j.ymssp.2017.02.010.